Numerical analysis of field geosynthetic-reinforced retaining walls with secondary reinforcement

Y. JIANG*, J. HAN†, J. ZORNBERG‡, R. L. PARSONS†, D. LESHCHINSKY§ and B. TANYU∥

Geosynthetic-reinforced retaining (GRR) walls typically have vertical reinforcement spacing of 0·6 m, and this relatively large spacing has been known to cause comparatively high connection forces. To reduce this connection force, short geosynthetic reinforcement layers (referred to as secondary reinforcement layers) are installed between blocks where there are no primary reinforcement layers. This paper presents two-dimensional numerical simulations that were developed to analyse an instrumented GRR wall with secondary reinforcement layers in the field. A finite differential software was employed to develop the numerical model. In addition to the Mohr–Coulomb model, the cap yield model based on the theory of hardening plasticity was used to represent the behaviour of backfill. Inclinometer casings, earth pressure cells and strain gauges were installed in the instrumented GRR walls to measure the facing deflections, lateral earth pressures, vertical earth pressures and geogrid strains. The measured results and numerical predictions were compared and discussed, and reasonable agreement between these results was found. Compared to the measured results, the numerical predictions slightly underestimated the maximum wall facing deflections and vertical earth pressures, and slightly overestimated lateral earth pressures and strains in primary and secondary reinforcement layers. For comparison, a numerical model without secondary reinforcement was developed as well. This comparison revealed that the GRR wall with secondary reinforcement resulted in smaller facing deflections and maximum strains in primary reinforcement layers. Overall, the numerical analysis indicated that secondary reinforcement could provide clear benefits in improving the performance of GRR walls.

KEYWORDS: deformation; field instrumentation; numerical modelling; retaining walls; stress analysis

INTRODUCTION

Geosynthetic-reinforced retaining (GRR) walls have been used extensively in transportation and residential projects. Han (2015) identified the benefits of using such wall systems. The American Association of State Highway and Transportation Officials (AASHTO, 2014) and the British Standards Institution (BS 8006-1:2010+A1:2016 (BSI, 2016)) have developed design guidelines for such GRR walls. The vertical spacing of geosynthetic reinforcement layers in a GRR wall is typically 0·6 m. This relatively large spacing can cause comparatively high connection forces near the back of the wall facing, and even bulging of the wall facing. To mitigate such problems, additional short geosynthetic reinforcement layers (referred to as secondary reinforcement layers) are installed between primary geosynthetic reinforcement layers, as shown in Fig. 1.

Analytical and experimental studies have been performed on GRR walls with secondary reinforcement layers (Leshchinsky, 2000; Han & Leshchinsky, 2006; Leshchinsky *et al.*, 2014; Jiang *et al.*, 2015, 2016). For example, Leshchinsky (2000) reported that the use of secondary

reinforcement layers could mitigate the problems resulting from the relatively large vertical spacing of primary reinforcement layers in GRR walls. Han & Leshchinsky (2006) and Leshchinsky *et al.* (2014) used a limit equilibrium method to investigate the effect of secondary reinforcement on the behaviour of GRR walls. Based on the results from centrifuge models and associated limit equilibrium analyses, Zornberg *et al.* (1998a, 1998b) concluded that secondary reinforcements played a significant role in the overall stability of geosynthetic-reinforced soil structures. In addition to analytical studies of GRR walls with secondary reinforcement layers, Jiang *et al.* (2015, 2016) performed field tests to investigate the effect of secondary reinforcement on GRR wall performance. These results confirmed that the secondary reinforcement could reduce the lateral deformation of the wall facing, the connection load and the tensile load in the primary reinforcement layers.

Compared with analytical and experimental studies, numerical simulations can provide evaluations on a comparatively wider range of parameter values and, consequently, more comprehensive results. Extensive studies have been conducted to evaluate the behaviour of GRR walls (e.g. Christopher *et al.*, 1989; Ho & Rowe, 1996; Ling & Leshchinsky, 2003; Hatami & Bathurst, 2006; Guler *et al.*, 2007; Huang *et al.*, 2009, 2011, 2013; Mirmoradi & Ehrlich, 2014; Yu *et al.*, 2016; Zheng & Fox, 2016). In particular, Ling & Leshchinsky (2003) used two-dimensional finite-element simulations to investigate the behaviour of GRR walls. In their numerical model, a non-linear hyperbolic model proposed by Duncan *et al.* (1980) was used to simulate the behaviour of backfill. The numerical results showed that a decrease in the vertical reinforcement spacing reduced wall facing deflections and maximum tensile loads in reinforcement layers, but increased lateral pressure behind the wall.
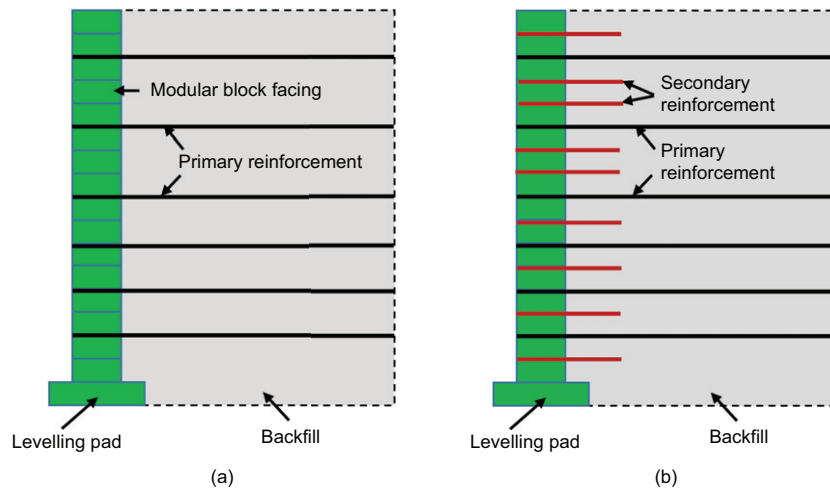
Fig. 1. Cross-section of GRR walls: (a) without secondary reinforcement layers; (b) with secondary reinforcement layers

Similarly to Ling & Leshchinsky (2003), Hatami & Bathurst (2006) evaluated the influence of backfill compaction and reinforcement type on the performance of GRR walls using the fast Lagrangian analysis of continua (FLAC), a two-dimensional finite-difference program. Using a three-dimensional finite difference program, FLAC3D, Huang *et al.* (2011) conducted numerical analyses to assess the behaviour of a laterally loaded shaft constructed within a GRR wall. Based on the Huang *et al.* (2011) study, Huang *et al.* (2013) refined the numerical model by: (*a*) using the cap yield (CY) model for backfill; (*b*) introducing interfaces between discrete facing blocks; and (*c*) considering compaction for backfill. The results from the refined model better matched those from field monitoring.

Although extensive numerical studies have been performed on GRR walls, very few have been performed on GRR walls with secondary reinforcement layers. Only Leshchinsky & Vulova (2001) have investigated the influence of secondary reinforcement on failure modes of GRR walls. Their study illustrated that the inclusion of secondary reinforcement could reduce the connection load in the primary reinforcement, increase internal wall stability and change the failure mode from reinforcement connection failure to compound failure.

In this study, a two-dimensional numerical model was developed using FLAC to analyse an instrumented GRR wall with secondary reinforcement layers. The CY model was employed to simulate the behaviour of backfill. The geosynthetic reinforcement was modelled as a linearly elastic–perfectly plastic material limited by its tensile strength, which was characterised as the yield strength. The block–block interface, block–backfill interface, backfill–geosynthetic reinforcement interface, compaction-induced stress and construction procedures of GRR walls with secondary reinforcement were also considered in this study. The wall facing deflections, lateral earth pressures, vertical earth pressures and strains in reinforcement layers from the field test and the numerical simulation are compared and discussed. For comparison, an additional numerical model was built to simulate a GRR wall without secondary reinforcement layers. In summary, although significant advances have been made regarding the use of numerical simulations in GRR walls, their use to investigate the effect of secondary reinforcements has been, at best, limited. This is certainly the case for numerical simulation that involved the comparison of numerical predictions against field monitoring results.

BRIEF DESCRIPTION OF INSTRUMENTED GRR WALL

The GRR wall evaluated in this study is located at Bonner Springs, Wyandotte County, Kansas, USA, and was constructed to support a new ramp for the Kansas Department of Transportation I-70/K-7 interchange project. The longitudinal length of the GRR wall is 353 m, of which a portion was designated as the test wall. Three wall sections were selected to be instrumented for field tests. In this paper, a test wall section with uniaxial geogrid as primary reinforcement and biaxial geogrid as secondary reinforcement was selected for the numerical simulation. This was because the instrumentation in this section was more comprehensive than that in the other two test wall sections.

Figure 2 shows a cross-section of the instrumented wall. The wall was constructed on bedrock and had modular block facing. Four types of high-density polyethylene uniaxial geogrids were used as primary reinforcement and a polypropylene biaxial geogrid was used as secondary reinforcement. The lengths of the primary and secondary reinforcement layers were 18·0 to 18·3 m and 1·3 m, respectively. The backfill for the instrumented walls was gravel. The backfill was compacted with a lift thickness of 0·2 m. A light plate compactor was used to compact the backfill within 1 m behind the wall facing and a heavy roller compactor was used to compact the backfill at 1 m away from the wall facing. The primary geogrid layers were installed every two blocks (i.e. 0·4 m) in the lower third of the wall, and every three blocks (i.e. 0·6 m) in the upper two-thirds of the wall. A 4(H):1(V) backslope was constructed on the top of the wall.

The instrumentation was installed during the construction of the wall and its layout is shown in Fig. 2. Wall facing deflections, lateral earth pressures at the back of the wall facing, vertical earth pressures at the bottom of the wall and strains in primary and secondary reinforcement layers were measured during the construction. Details of the instrumentation can be found in Jiang *et al.* (2016).

NUMERICAL MODELLING
Geometry and boundary conditions

A two-dimensional (2D) numerical model was developed to analyse the instrumented wall. A 2D evaluation was selected because the wall length was approximately eight times larger than the length of the secondary reinforcement layers, which is typically required by a plane-strain condition. Fig. 3 shows the mesh of the numerical model. The entire
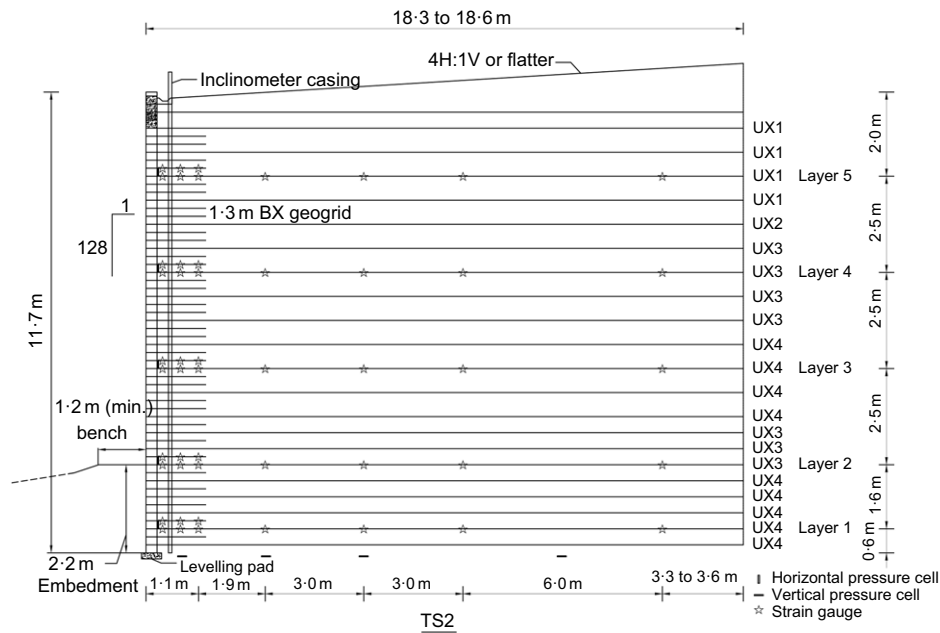
Fig. 2. Cross-section of instrumented wall (Jiang *et al.* (2016), with permission from ASCE)
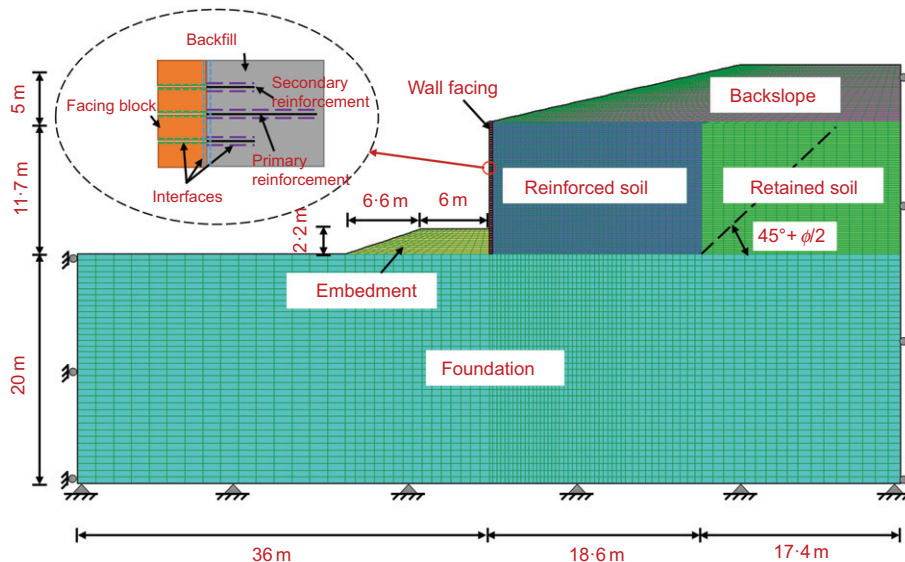
Fig. 3. Mesh of the numerical model

numerical model mainly included a foundation, embedment soil, wall facing, a reinforced soil zone, a retained soil zone and a backslope. The foundation was 20 m thick and 72 m long. The foundation in front of the wall facing was extended to 36 m to minimise the boundary effects on the numerical simulations.

The height of the wall facing in the numerical model was 11·7 m, containing 58 stacked facing blocks and a wall cap that were 0·2 and 0·1 m high, respectively. The width of the wall facing was 0·3 m. The reinforced soil zone was 18·3 m wide and 11·5 m high. The retained soil zone was 11·7 m high. To minimise boundary effects, the width of the retained soil zone was extended to 17·4 m. The embedment in front of the wall facing was constructed in two stages. The embedment in the numerical model was simulated as a right angle trapezoid. The height and upper width of the embedment were 2·2 and 6 m, respectively. The side slope of the embedment zone had a ratio of 3(H):1(V). The backslope

was 5 m high starting from the back of the wall facing and extending upward, with an approximate slope ratio of 4(H):1 (V). As shown in Fig. 3, the bottom of the model was fixed vertically and horizontally; the left and right sides were fixed horizontally, but set to be free vertically.

Soil constitutive models and properties

Two constitutive models were used to simulate the behaviour of the backfill: the Mohr–Coulomb (MC) model and the CY model. The MC model represented a linearly elastic–perfectly plastic material with the MC failure criterion; the parameters for this model are listed in Table 1.

The MC model as well as other soil constitutive models (e.g. a non-linear hyperbolic model proposed by Duncan *et al.* (1980)) have been used in the simulation of GRR walls (e.g. Hatami & Bathurst, 2006; Huang *et al.*, 2009; Yu *et al.*, 2016). However, compared with those models, the CY model

Table 1. Parameters in the numerical model

Material	Constitutive model	Unit weight: kN/m^3	Young's modulus: MPa	Poisson ratio	Cohesion: kPa	Friction angle: deg	Dilation angle: deg
Backfill	Mohr–Coulomb	18·1	20	0·2	0	52	8
Retained soil/backslope/embedment soil	Mohr–Coulomb	16·8/20·0*	20	0·3	1	34	0
Foundation bedrock	Linearly elastic	20·0	2000	0·2	0	0	0
Block facing	Linearly elastic	15·0	2000	0·25	—	—	—

*The unit weight of backslope was assumed to be 20·0 kN/m^3.

was developed based on the theory of hardening plasticity (Itasca, 2011) and has the following capabilities: (*a*) to model the hardening behaviour of volumetric strain under isotropic compression; (*b*) to simulate soil modulus decrease and plastic deformation subjected to shear loading; and (*c*) to exhibit dilative characteristics.

As shown in Fig. 4, the CY model has two yield surfaces in p'–q space: (*a*) a CY surface and (*b*) a shear yield surface. An associated flow rule is used for the CY surface, whereas a non-associated flow rule is adopted for the shear yield surface. Fig. 5 shows the measured relationship between the volumetric strain and the isotropic compressive stress of the backfill, which was used to determine the parameters for the CY model. The details of the CY model are delineated in the FLAC manual of the constitutive model (Itasca, 2011).

The friction angle of the backfill was determined by three triaxial compression tests. As the numerical simulation of the instrumented wall was under a plane-strain condition, a correlation for cohesionless soils recommended by Kulhawy & Mayne (1990) was used to calculate the plane-strain friction angle as follows: $\phi_s = 1·12\phi_{tc} = 52°$, where ϕ_s is the friction angle in the plane strain condition and ϕ_{tc} is the friction angle from triaxial compression tests.

The dilation angle in the numerical simulation was determined using the equation given by Vermeer & de Borst

(1984) for granular materials. The CY surface parameter, α, and the plastic strain coefficient, β, were calibrated by matching a stress–strain curve of the triaxial compression test at a confining stress of 200 kPa, as shown in Fig. 6(a). Table 2 summarises the CY model parameters for the backfill.

Figure 6 shows a comparison between the results from the triaxial compression tests and numerical predictions. The friction angle of a granular material depends on the confining stresses. In practice, however, a straight MC failure line, which is not dependent on confining stresses, is often used to characterise the shear strength of the material. This approach was also adopted in this study. It is not surprising that there are some differences between the experimental data and numerical results. However, in this study, comparisons of the results focused primarily on strain levels below 2%, as this was the strain level observed in the field. Fig. 6(a) shows very good agreement between the experimental and numerical results within this strain level.

The results from the isotropic compression test and the numerical simulation are also compared in Fig. 7. A notable divergence can be seen between the results from the
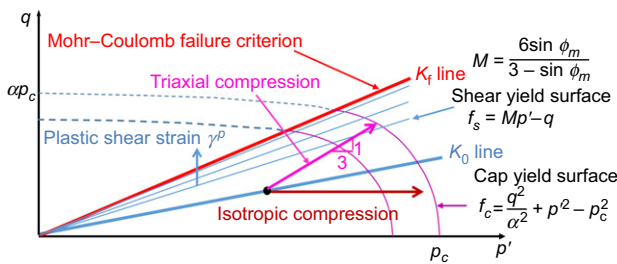
Fig. 4. Yield surfaces of the CY model in p'–q space
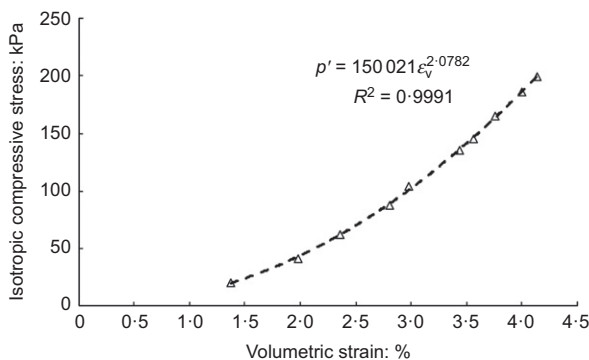
Fig. 5. Power function for the relationship between volumetric strain and isotropic compressive stress
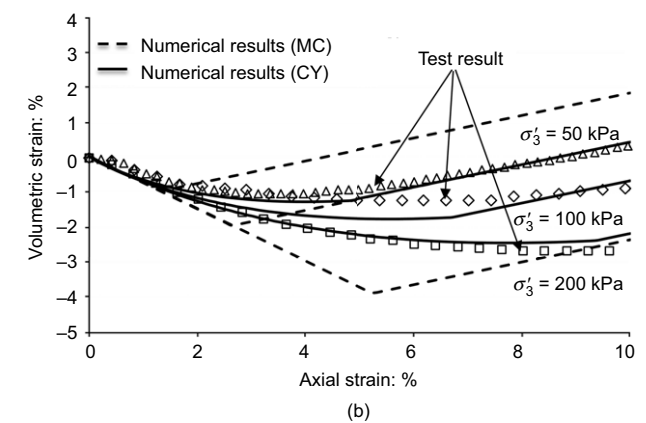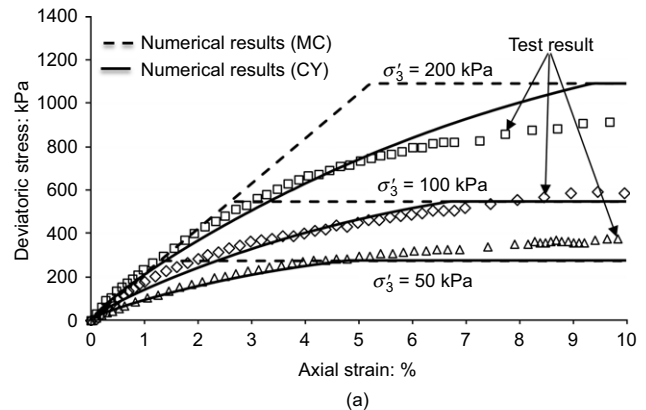
Fig. 6. Numerical simulation of triaxial compression tests on the backfill using MC model and CY models: (a) stress–strain relationship; (b) volumetric–axial strain relationship

numerical simulation using the MC model and the isotropic compression test, whereas the results from the numerical simulation using the CY model agreed well with those from the isotropic compression test. The above comparisons demonstrate that the parameters for the CY model were successfully determined, calibrated and verified.

The facing blocks and the foundation bedrock were modelled as linearly elastic materials and their properties are summarised in Table 1. The retained soil together with the backslope and embedment soils were modelled using the MC model to simulate their behaviour and Table 1 presents their parameters. The parameters of the retained soil in this study were assumed to be the same as those used by Huang *et al.* (2011) because these soils are from the same area.

Reinforcement constitutive models and properties

The numerical simulation in this study used strip elements for the reinforcement layers. The reinforcement was assumed to be a linearly elastic–perfectly plastic material, allowing for small deformations. The secant stiffness of the geogrid at 2% strain (1000 h creep strain) based on the laboratory evaluation of geosynthetic reinforcement (NTPEP, 2011) was selected as the constant stiffness for the numerical simulation. Tensile strain at failure was assumed to be 10%, and the yield strengths of the geogrids were the same as those provided by the manufacturer. Table 3 summarises the parameters of reinforcement in the numerical simulation.

Interface properties

Four types of interfaces were considered in the numerical model: (*a*) the backfill–reinforcement interface; (*b*) the block–block interface; (*c*) the block–backfill interface; and (*d*) the block–embedment soil interface. These interfaces were modelled as linearly elastic–perfectly plastic with the MC failure criterion. The interface shear stress linearly increases with an increase in relative displacement and starts to yield at the maximum shear stress. Equation (1) gives the formula to calculate the maximum shear stress

$$\tau_{max} = c_{int} + \sigma'_n \tan \phi'_{int} \tag{1}$$

where c_{int} is the interface cohesion; σ'_n is the effective normal stress; $\phi'_{int} = \tan^{-1}(c_{rf}\tan\phi)$ denotes the friction angle of the interface; c_{rf} is the reduction factor; and ϕ is the friction angle of the soil.

Table 4 summarises the interface properties used in this study. The reduction factors c_{rf} of 0·67 and 0·84 were used to calculate the backfill–reinforcement interface friction angles for the uniaxial geogrid and the biaxial geogrid, respectively. The dilation angle and cohesion of the backfill–reinforcement interface were assumed to be zero. A pullout test was used to calibrate the shear stiffness of the backfill–reinforcement interface.

The shear resistance between facing blocks mainly results from: (*a*) surface friction between facing blocks and (*b*) cohesion due to a connector serving as a shear key. The block–block interface properties were determined by referring to block–block shear test results in Hatami & Bathurst (2006). The properties of the interface between the levelling pad (assuming the same size as the block) and the foundation were assumed to be the same as those of the block–block interface.

The friction angles of the block–backfill interface and the block–embedment interface were calculated using $c_{rf} = 0·67$. The dilation angle and cohesion for the block–backfill interface were assumed to be 8° and 0 kPa, respectively. The interface normal and shear stiffness values were assumed to be the same as those used by Hatami & Bathurst (2006) because both studies used concrete modular blocks and granular materials for the backfill soils.

Modelling procedures

The numerical model simulated construction procedures as follows: (*a*) prior to wall construction, the foundation

Table 2. Parameters for the CY model of the backfill

Parameters	Unit	Value
Unit weight, γ	kN/m³	18·1
Cap yield surface parameter, α	—	1·5
Friction angle, ϕ	deg	52
Dilation angle, ψ	deg	8
Multiplier, R	—	6·2
Plastic strain coefficient, β	—	0·5
Reference elastic tangent shear modulus, G^e_{ref}	kPa	32 500
Reference bulk modulus, K^{iso}_{ref}	kPa	6971
Reference pressure, P_{ref}	kPa	100
Poisson ratio, v_{ur}	—	0·2
Cohesion, c	kPa	0
Power, m	—	0·52
Failure ratio, R_f	—	0·9
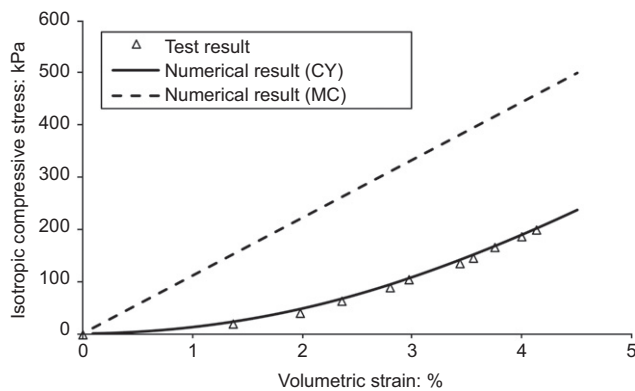
Fig. 7. Numerical simulation of isotropic compression test on the backfill using MC model and CY models

Table 3. Parameters of geogrid in numerical modelling

Materials	Structure element type	Constitutive model	Secant stiffness at 2%, $J_{@2\%}$: kN/m	Yield strength: kN/m	Tensile failure strain: %
UX1	Strip	Linearly elastic and perfectly plastic	360	58	10
UX2			407	70	10
UX3			637	114	10
UX4			860	144	10
BX			330*	19	10

*Stiffness in the cross-machine direction.

Table 4. Interface parameters

Interface	Friction angle: deg	Dilation angle: deg	Cohesion: kPa	Normal stiffness, k_n: MN/m/m	Shear stiffness, k_s: MN/m/m
Backfill–reinforcement	40/47*	0	0	—	6·5
Block–block	57	0	46	1000	40
Block–backfill	40	8	0	100	1
Block–embedment soil	28	0	0	100	1

*40° is for uniaxial geogrid and 47° is for biaxial geogrid.

bedrock reached an equilibrium under gravity; (*b*) a layer of the wall facing, backfill and retained soil was placed in the numerical model; (*c*) primary and secondary reinforcement layers were installed and connected to the facing blocks; (*d*) corresponding interfaces were activated; (*e*) a vertical compaction stress was applied on the top of the reinforced soil; (*f*) the numerical model was solved to reach a new equilibrium; (*g*) steps (*b*) to (*f*) were repeated up to the top of the wall; and (*h*) the backslope was constructed on the top of the wall.

The wall was built in lifts on a rigid foundation. To numerically simulate this construction procedure, a reinforced soil layer was activated without any settlement and compaction stresses were applied on top of this layer. The self-weight of the reinforced soil and the compaction stresses induced settlement after the numerical simulation reached equilibrium. After reaching equilibrium, the next reinforced soil layer was activated without settlement and compaction stresses were applied on the top of the new layer. The self-weight of the new layer and the new compaction stresses would induce settlements not only in the new layer, but also in the previous layer(s). This procedure was continued until all reinforced soil layers were placed. As the settlements of the previous layers accumulated under the placement of new layers, and the new layer did not have any settlement at the moment of placement, maximum settlements occurred at approximately the mid-height of the wall.

The numerical simulation was conducted using the small-strain mode in the software because the wall was under a working condition, and the measured wall facing deflections and reinforcement strains were comparatively small. A large-strain mode was used to analyse one case to verify the selection of the small-strain mode. The numerical results using the large-strain mode were almost identical to those using the small-strain mode; therefore, the selection of the small-strain mode was confirmed. Each reinforcement layer was connected to the facing block through a pin connection. The simulation of compaction stress is a challenge as there is no widely accepted method to do this. Hatami & Bathurst (2006) and Guler et al. (2007) modelled compaction stress by applying an 8 kPa distribution pressure on the top of each lift. Mirmoradi & Ehrlich (2014) modelled a compaction stress by applying an 8 kPa distribution stress at the top and bottom of each soil layer. Huang et al. (2013) simulated the effect of compaction stress by applying an additional lateral stress of 10 kPa to each lift by way of a heavy compactor, or 8 kPa by way of a light compactor. Yu et al. (2016) modelled compaction stress by applying two – 8 kPa and 16 kPa – distribution pressures on the top of each lift separately, for the same wall. The compaction stress in this study was modelled by applying an 8 kPa distribution pressure on the top of each lift. A more accurate simulation of compaction stress and investigation into the effect of the compaction stress level require further study, but they are beyond the scope of this study.

NUMERICAL RESULTS AND DISCUSSION
Wall facing deflection

The wall facing deflection from the numerical simulation was the deflection that occurred after the placement of the facing block. In other words, the deflection at a given wall height started at the moment when the wall construction reached that height. This approach has also been adopted in other studies – for example, Hatami & Bathurst (2006) and Yu et al. (2016). In the following sections, the wall facing deflections are used for the convenience of presentation.

The wall facing deflections predicted by the numerical simulation and measured in the field test before and after construction of the backslope are shown in Figs 8(a) and 8(b), respectively. Both figures show that the deflections measured in the field test increased to the maximum and then decreased along the wall height. The deflections approached the maximum value at approximately the middle of the wall height. Although the maximum deflections predicted by the numerical simulation were slightly smaller than those from the field test, the deflections predicted by the numerical simulation captured the overall trend of the measured deflections. Guler et al. (2007), Huang et al. (2009) and Yu et al. (2016) also found similar trends along the wall height. After backslope construction, an increase in wall facing deflections can be observed in both the field test and the numerical simulation. This increase resulted from the weight of the backslope and the induced lateral earth pressure.

A comparison of wall facing deflections predicted by the numerical simulation using the MC and CY models can also be seen in Fig. 8. Overall, the deflections predicted by the numerical simulation using the CY model were closer to the measured one than that using the MC model. Also, the CY
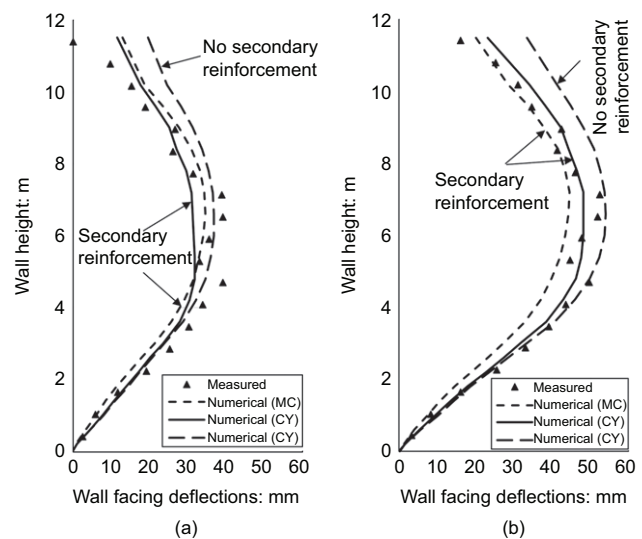
Fig. 8. Wall facing deflections: (a) before construction of the backslope; (b) after construction of the backslope

model led to larger wall facing deflections than the MC model. This is because the mobilised friction angle (ϕ_m) in the CY model was lower than the friction angle in the MC model. The soil yielded at the low strain level when the CY model was used. The difference in the deflections between the MC and CY models became larger after backslope construction because the soil modulus in the CY model further decreased due to shear stresses induced by the backslope, while the soil modulus in the MC model remained constant.

A GRR wall identical to that shown in Fig. 3, but without secondary reinforcement layers, was also numerically modelled using the CY model for comparison, as shown in Fig. 8. It can be seen that the GRR wall without secondary reinforcement layers had larger wall facing deflections in the upper two-thirds of the wall height than that with secondary reinforcement layers. This demonstrates that the secondary reinforcement resulted in a reduction in wall facing deflections. This benefit increased after construction of the backslope. In Fig. 8, this reduction in the deflections in the lower third of the wall is almost imperceptible, as the vertical spacing of the primary reinforcement is only 0·4 m, which is too close to show the benefits of the secondary reinforcement.

Lateral earth pressures

The numerical simulation predicted the lateral earth pressures before and after construction of the backslope, as shown in Fig. 9. For comparison, the lateral earth pressures predicted using the Rankine active earth pressure theory and the at-rest earth pressure are also shown in Fig. 9. The lateral earth pressures predicted by the numerical simulation above the embedment zone increased approximately linearly with depth and were close to the Rankine active earth pressures. In the numerical simulation, the lateral earth pressure from the top of the embedment zone to the bottom of the wall increased substantially, and then approached the at-rest earth pressure at the bottom of the wall. This is because the embedment soil in front of the wall restricted the development of wall facing deflections within the embedment zone so that the lateral earth pressure within the embedment zone was close to the at-rest earth pressure. Above the embedment zone, the lateral earth pressures predicted by the numerical simulation showed a reasonable agreement with those from the field test. Fig. 9 shows that the measured lateral earth
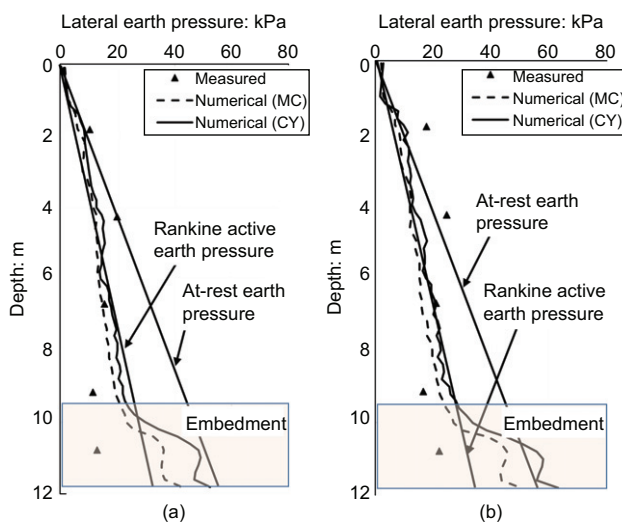
pressures were comparatively large near the top of the wall, likely because the wall facing deflections were comparatively small near the wall top due to the later placement of fill materials. As a result, the active lateral earth pressures were not fully mobilised at this location. Also, the measured lateral earth pressure at the locations within the embedment deviated from the numerical result and at-rest earth pressure. This deviation may result from the soil arching effect due to the stiffness difference between the wall facing and the backfill, which resulted in a lower vertical stress.

The results from the field test and numerical simulation showed the increased pressures due to construction of the backslope. Fig. 9 also shows that the lateral earth pressures predicted using the CY model are almost the same as those using the MC model. The pressures predicted for the GRR wall without secondary reinforcement were nearly the same as those for the GRR wall with secondary reinforcement, and therefore the lateral earth pressures predicted for the wall without secondary reinforcement are not shown in Fig. 9.

Vertical earth pressures

Figure 10 shows the distributions of vertical earth pressure at the bottom of the wall from the field test and the numerical simulation, as well as those calculated using the simplified methods. The vertical pressures from the numerical simulation decreased at the back of the wall facing owing to the soil arching effect between the wall facing and the backfill soil. The reinforced soil behind the back of the wall facing was subjected to upward friction because the reinforced soil settled more than the wall facing, which then reduced the vertical earth pressure at the bottom of the wall. The overburden stress calculated by the simplified method is the unit weight of the soil multiplied by the depth. The trapezoid stress was calculated by considering the reinforced zone as a
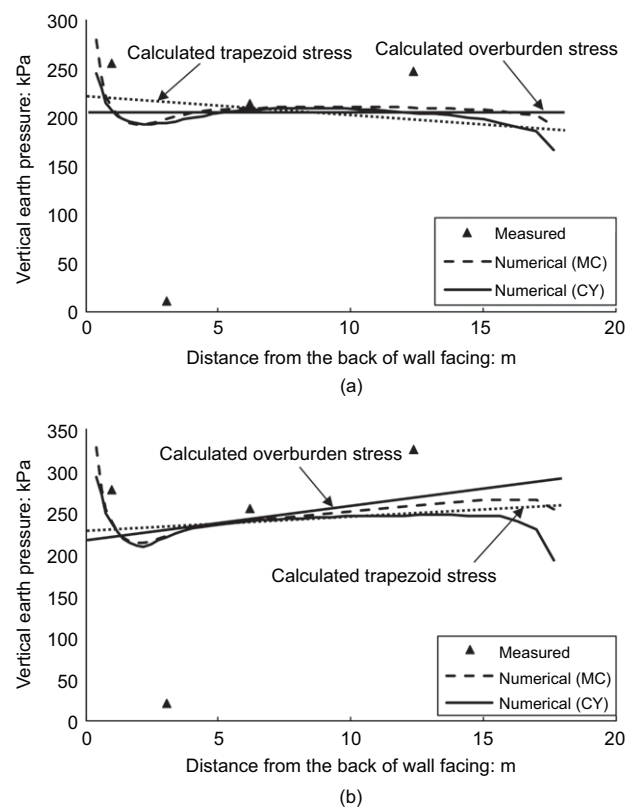
Fig. 10. Vertical earth pressure: (a) before construction of the backslope; (b) after construction of the backslope

Fig. 9. Lateral earth pressure: (a) before construction of the backslope; (b) after construction of the backslope

rigid body subjected to a lateral earth pressure from the retained soil. However, the effect of friction was not considered in the simplified methods to calculate the trapezoid and overburden stresses. After the sudden drop, the vertical earth pressure at the bottom of the wall reached a relatively constant value before construction of the backslope and then gradually increased after the construction of the backslope. As indicated by Jiang *et al.* (2016), the second measured point from the left was not reliable, potentially due to the malfunction of this earth pressure cell. Although the vertical earth pressures predicted by the numerical simulation slightly underestimated those measured from the field test, the predicted and measured pressures reasonably corresponded, as did the calculated trapezoid stresses.

Figure 10 also shows that the CY model predicted slightly lower vertical pressures than the MC model. Since the vertical earth pressures predicted at the bottom of the wall were almost the same for the GRR walls with and without secondary reinforcement, the pressures for the GRR wall without secondary reinforcement are not shown in Fig. 10.

Strains in reinforcement layers

Figure 11 presents the strain distribution in the primary reinforcement layers at five instrumented layers (see Fig. 2) after the construction of the backslope. Positive strains indicate tension in the reinforcement layers, while negative strains indicate compression. The predicted strains at each instrumented layer quickly decreased from the back of the wall facing and gradually decreased to zero. Both field test and numerical simulation show negative strains appeared in the rear segment of the primary reinforcement layers because the reinforced soil was compressed by lateral earth pressure from the retained soil. Overall, the numerically predicted strains in the primary reinforcement layers reasonably tracked the measured strain distribution from the field test. In addition, the maximum tensile strain distribution along the wall height matched well with the wall facing deflection distribution. Also, the tensile strains predicted in the primary reinforcement layers using the MC model were smaller than those using the CY model.

Figure 11 also shows the strains predicted in the primary reinforcement layers using the CY model for the GRR wall without secondary reinforcement. The maximum tensile strain occurred at the connection and was followed by a rapid decrease in the GRR wall without secondary reinforcement. However, a different distribution was found in the wall with secondary reinforcement. For example, the maximum tensile strains in layers 2, 3 and 4 occurred at the end of the zone reinforced with secondary reinforcement layers. Compared with the GRR wall without secondary reinforcement, the tensile strain distribution of the primary reinforcement in the GRR wall with the secondary reinforcement was altered within the secondary reinforcement zone except for layer 1. The tensile strain at the connection was reduced by the secondary reinforcement layers. The placement of secondary reinforcement layers could be considered a reduction of reinforcement spacing. Since the secondary reinforcement carried tensile forces near the wall facing, the forces required for the primary reinforcements to maintain stability of the wall facing became smaller. As a result, the secondary reinforcements resulted in a reduction in the connection stresses in the primary reinforcement.

Figure 12 presents the distribution of tensile strain in the secondary reinforcement layers after construction of the backslope. Overall, the strains predicted at each instrumented layer decreased quickly behind the back of the wall facing. The maximum strains in the secondary reinforcement calculated by the numerical simulation occurred at the
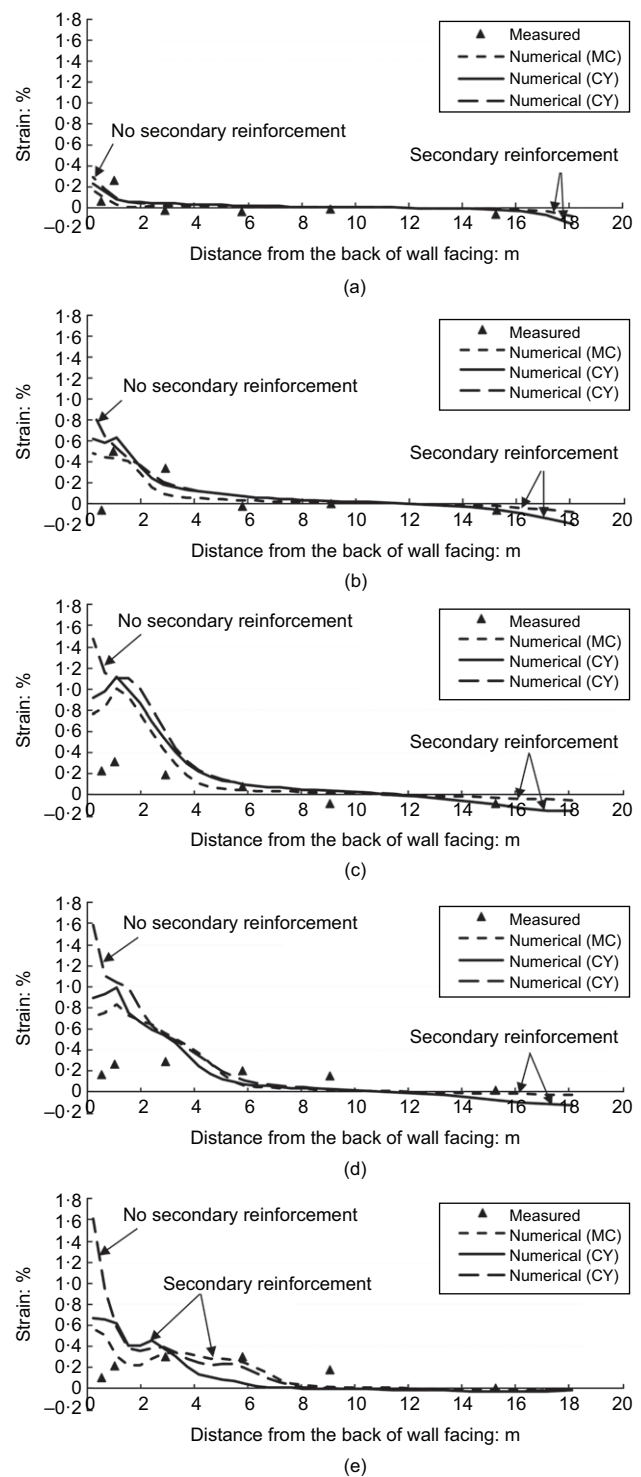
Fig. 11. Distribution of strains in primary reinforcement layers: (a) layer 1; (b) layer 2; (c) layer 3; (d) layer 4; (e) layer 5

connection. The measured tensile strains near the wall facing were lower than the calculated ones from the numerical simulation because the middle portion of the connector during the construction might not be in tight contact with the block and the measured strains in the reinforcement near the wall facing were relatively low. The predicted tensile strains away from the wall facing from the numerical simulation were close to the measured ones. Overall, there was a reasonable agreement between the strains predicted by the numerical simulation and those measured in the field test. Again, the tensile strains predicted using the CY model were larger than those in the MC model.
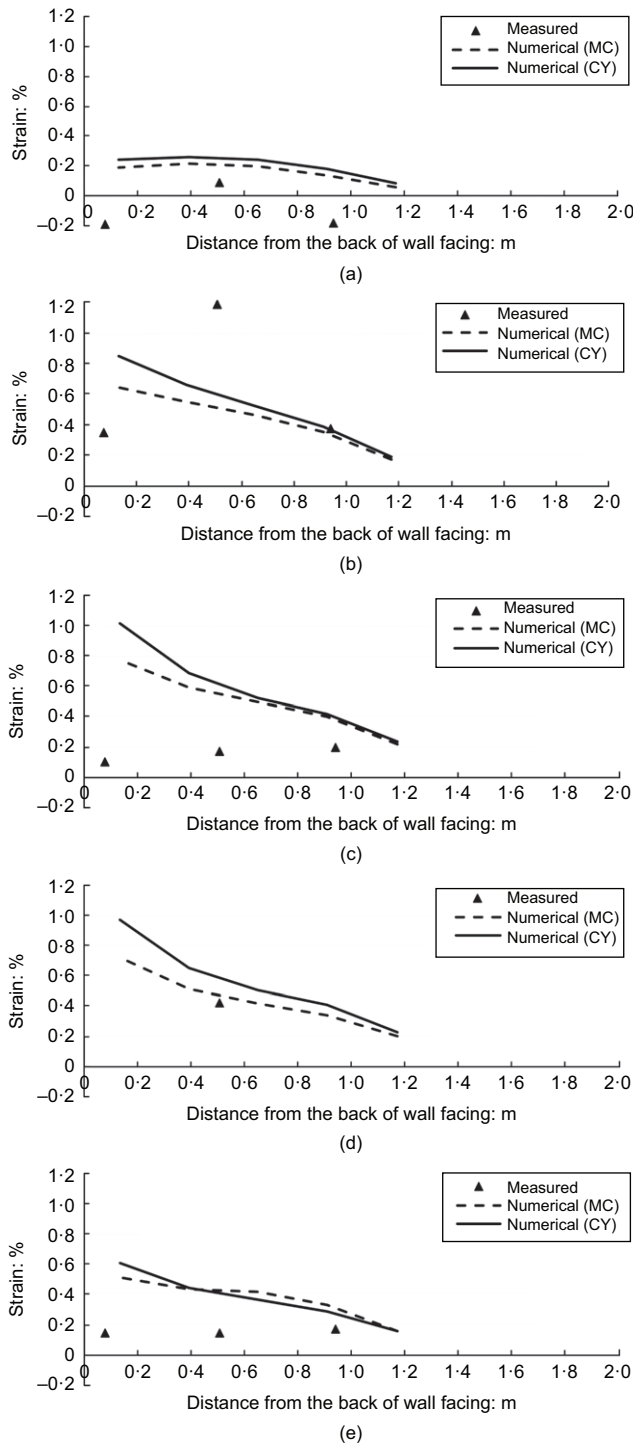
Fig. 12. Distribution of strains in secondary reinforcement layers: (a) layer a; (b) layer b; (c) layer c; (d) layer d; (e) layer e

Fig. 13. Distribution of maximum tensile stress

Stresses in primary reinforcement layers

Figure 13 shows the distribution of maximum tensile stresses in the primary reinforcement layers from the field test and the numerical simulation, after the construction of the backslope. As shown in Fig. 13, the maximum tensile stress from the numerical simulation increased with depth and reached its greatest value at approximately the middle of the wall. Thereafter, the maximum tensile stress decreased with depth toward the bottom of the wall. There were two reasons for the decrease in the maximum tensile stress in the primary reinforcement layer in the lower part of the wall: (*a*) the vertical spacing of the primary reinforcement became smaller
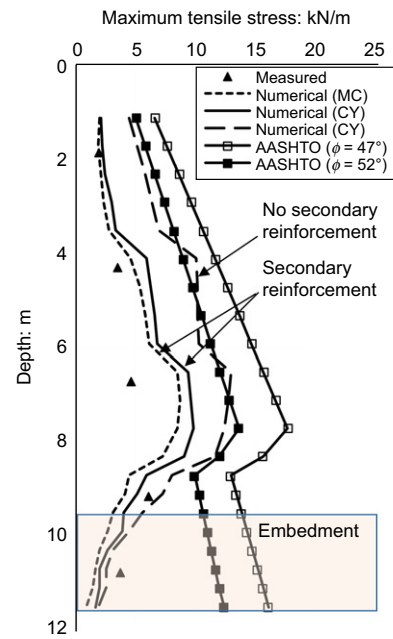
and (*b*) the embedment limited the development of wall facing deflection. The numerically predicted maximum tensile stress tracked the maximum tensile stress distribution along the depth of the wall from the field test, although the values from the numerical simulation were slightly higher. Furthermore, the maximum tensile stresses in the primary reinforcement layers were higher using the CY model than the MC model because of the decreased soil modulus in the CY model.

For comparison, the distribution of maximum tensile stresses for the GRR wall without secondary reinforcement is also presented in Fig. 13. The maximum tensile stresses for this case were higher than those for the wall with secondary reinforcement. This result indicates again that the secondary reinforcement reduced the maximum tensile stresses in the primary reinforcement layers. The AASHTO simplified method (AASHTO, 2014) was employed to calculate the maximum tensile stresses in the primary reinforcement layers, as shown in Fig. 13. Two friction angles, 47° and 52°, were used in the calculation for the following reasons: (*a*) a friction angle of 47° was obtained from triaxial compression tests, and the AASHTO simplified method recommends the use of the shear strength from triaxial compression tests; (*b*) a friction angle of 52° was converted for the plane-strain condition and was used in the numerical simulation. As shown in Fig. 13, in the upper two-thirds of the wall, the maximum tensile stresses calculated using the AASHTO simplified method captured the trend of maximum tensile stresses from the numerical simulation; also, the maximum tensile stresses calculated using the friction angle of 52° agreed well with those from the numerical simulation for the wall without secondary reinforcement. However, in the lower third of the wall, the maximum tensile stresses from the numerical simulation decreased with depth, whereas the maximum tensile stresses calculated using the AASHTO simplified method increased with the depth. This result can be attributed to the conservatism of the AASHTO simplified method, as it ignores the effect of toe resistance, which results in the reduced maximum tensile stress.

It should be noted that only a few secondary reinforcement layers in the lower portion of the wall intercept the potential Rankine failure surface. In the field study as well as the

numerical simulation, the wall was embedded and the soil in front of the wall minimised wall movement and prevented the possible development of this surface. As a result, the measured earth pressures in the lower portion of the wall were close to the at-rest lateral earth pressure values. The numerical results show that the secondary reinforcements in the lower portion of the wall did not reduce the tensile stresses in the primary reinforcement layers. The effect of secondary reinforcements on the tensile stresses in the primary reinforcements would be more significant if the wall had not been embedded and had been close to its limit state.

The design procedure for considering the influence of the secondary reinforcement on the tensile stress in the primary reinforcement is provided in the research report by Jiang *et al*. (2015).

reinforcement layers at the connection were reduced by the secondary reinforcement layers.

(*f*) The numerically predicted maximum tensile stress tracked the maximum tensile stress distribution from the field test along the depth of the wall. The maximum tensile stress predicted using the AASHTO simplified method agreed well with results from the numerical simulation for a GRR wall without secondary reinforcement layers in the upper two-thirds of the wall. However, the maximum tensile stress calculated in the numerical simulation in the lower third of the wall decreased with depth, whereas the maximum tensile stress calculated using the AASHTO simplified method increased with depth. This can be attributed to the conservatism of the AASHTO simplified method, as it ignores the effect of toe resistance, which results in a reduced maximum tensile stress.

CONCLUSIONS

This study performed two-dimensional numerical simulations to analyse the results from an instrumented GRR wall constructed with secondary reinforcement layers. The CY model was used to simulate the behaviour of backfill. Parameters for the CY model were successfully determined, calibrated and verified by triaxial compression and isotropic compression tests. Wall facing deflections, vertical earth pressures, lateral earth pressures, strains in primary and secondary reinforcement layers, and maximum tensile stresses from the field test were compared with the predictions from the numerical simulation. For comparison, the same GRR wall without secondary reinforcement layers was also numerically modelled. The following conclusions can be drawn.

(*a*) Overall, the numerical simulation was found to adequately predict the behaviour of a GRR wall with secondary reinforcement layer in terms of the distribution of wall facing deflections, lateral and vertical earth pressures, and the strains in reinforcement layers.

(*b*) The numerical simulation using the CY model resulted in a better agreement with the field test results in aspects of the wall facing deflections than using the MC model. The numerical simulation using the CY model predicted larger wall facing deflections and strains in reinforcement layers than using the MC model; both of the models produced almost the same results for lateral and vertical earth pressures.

(*c*) The wall facing deflections for the wall without secondary reinforcement layers were found to be larger than those for the wall with secondary reinforcement layers. This result demonstrates that the use of secondary reinforcement leads to reduced wall facing deflections. However, the benefit of reduced wall facing deflection from secondary reinforcement was diminished by the closer vertical spacing of the primary reinforcement layers.

(*d*) The lateral earth pressures predicted by the numerical simulation above the embedment were found to be well represented by the Rankine active earth pressures. However, the lateral earth pressures predicted by the numerical simulation below the top of the embedment zone increased substantially, and then approached at-rest earth pressure at the bottom of the wall.

(*e*) Overall, the tensile strains in the primary reinforcement layers using the MC model were smaller than those using the CY model, especially at the locations close to the wall facing. The tensile strains in the primary

NOTATION

c_{int}	interface cohesion
c_{rf}	reduction factor
p'	mean effective stress
q	deviatoric stress
σ'_n	effective normal stress
τ_{max}	maximum shear stress of interface
ϕ	friction angle of soil
ϕ'_{int}	friction angle of interface
ϕ_m	mobilised friction angle of soil
ϕ_s	friction angle in the plane strain condition
ϕ_{tc}	friction angle from triaxial compression tests

REFERENCES

AASHTO (American Association of State Highway and Transportation Officials) (2014). *LRFD bridge design specifications*, 7th edn. Washington, DC, USA: AASHTO.

BSI (2016). BS 8006-1:2010+A1:2016 Code of practice for strengthened/reinforced soils and other fills. London, UK: BSI.

Christopher, B. R., Gill, S. A., Giroud, J. P., Juran, I. Scholsser, F., Mitchell, J. K. & Dunnicliff, J. (1989). *Reinforced soil structures, volume II. Summary of research and systems information*, Report No. FHWA-RD-89-043. Washington, DC, USA: Federal Highway Administration.

Duncan, J. M., Byrne, P. M., Wong, K. S. & Mabry, P. (1980). *Strength, stress–strain and bulk modulus parameters for finite element analyses of stresses and movements in soil masses*, Report No. UCB/GT/80-01. Berkeley, CA, USA: Department of Civil Engineering, University of California.

Guler, E., Hamderi, M. & Demirkan, M. M. (2007). Numerical analysis of reinforced soil-retaining wall structures with cohesive and granular backfills. *Geosynthetics Int.* **14**, No. 6, 330–345.

Han, J. (2015). *Principles and practice of ground improvement*. Hoboken, NJ, USA: John Wiley & Sons.

Han, J. & Leshchinsky, D. (2006). General analytical framework for design of flexible reinforced earth structures. *J. Geotech. Geoenviron. Engng* **132**, No. 11, 1427–1435.

Hatami, K. & Bathurst, R. J. (2006). Numerical model for reinforced soil segmental walls under surcharge loading. *J. Geotech. Geoenviron. Engng* **132**, No. 6, 673–684.

Ho, S. K. & Rowe, R. K. (1996). Effect of wall geometry on the behaviour of reinforced soil walls. *Geotextiles and Geomembranes* **14**, No. 10, 521–541.

Huang, B. Q., Bathurst, R. J. & Hatami, K. (2009). Numerical study of reinforced soil segmental walls using three different constitutive soil models. *J. Geotech. Geoenviron. Engng* **135**, No. 10, 1486–1498.

Huang, J., Parsons, R. L., Han, J. & Pierson, M. C. (2011). Numerical analysis of a laterally loaded shaft constructed within an MSE wall. *Geotextiles and Geomembranes* **29**, No. 3, 233–241.

Huang, J., Han, J., Parsons, R. L. & Pierson, M. C. (2013). Refined numerical modeling of a laterally-loaded drilled shaft in an MSE wall. *Geotextiles and Geomembranes* **37**, 61–73.

Itasca (2011). *FLAC: fast Lagrangian analysis of continua*, version 7.0. Minneapolis, MN, USA: Itasca Consulting Group, Inc.

Jiang, Y., Han, J., Parsons, R. L. & Cai, H. (2015). *Field monitoring of MSE walls to investigate secondary reinforcement effects*, Final Report, KDOT C1968. Topeka, KS, USA: Kansas Department of Transportation.

Jiang, Y., Han, J., Parsons, R. L. & Brennan, J. J. (2016). Field instrumentation and evaluation of modular-block MSE walls with secondary geogrid layers. *J. Geotech. Geoenviron. Engng* **142**, No. 12, https://doi.org/10.1061/(ASCE)GT.1943-5606. 0001573.

Kulhawy, F. H. & Mayne, P. W. (1990). *Manual on estimating soil properties for foundation design*, EPRI-EL-6800. Palo Alto, CA, USA: Electric Power Research Inst.

Leshchinsky, D. (2000). Alleviating connection load. *Geotech. Fabrics Rep.* **18**, No. 8, 34–39.

Leshchinsky, D. & Vulova, C. (2001). Numerical investigation of the effects of geosynthetic spacing on failure mechanisms of MSE block walls. *Geosynthetics Int.* **8**, No. 4, 343–365.

Leshchinsky, D., Kang, B. J., Han, J. & Ling, H. I. (2014). Framework for limit state design of geosynthetic-reinforced walls and slopes. *Transpn Infrastructure Geotechnol.* **1**, No. 2, 129–164.

Ling, H. I. & Leshchinsky, D. (2003). Finite element parametric study of the behavior of segmental block reinforced-soil retaining walls. *Geosynthetics Int.* **10**, No. 3, 77–94.

Mirmoradi, S. H. & Ehrlich, M. (2014). Numerical evaluation of the behavior of GRS walls with segmental block facing under working stress conditions. *J. Geotech. Geoenviron. Engng* **141**, No. 3, 1–8.

NTPEP (National Transportation Product Evaluation Program) (2011). *Laboratory evaluation of geosynthetic reinforcement*, National transportation product evaluation program, NTPEP Report 8507.4. Washington, DC, USA: American Association of State Highway and Transportation Officials.

Vermeer, P. A. & de Borst, R. (1984). Non-associated plasticity for soils, concrete and rock. *Heron* **29**, No. 3, 1–64.

Yu, Y., Bathurst, R. J. & Allen, T. M. (2016). Numerical modelling of the SR-18 geogrid reinforced modular block retaining walls. *J. Geotech. Geoenviron. Engng* **142**, No. 5, 04016003, https://doi.org/10.1061/(ASCE)GT.1943-5606.0001438.

Zheng, Y. & Fox, P. (2016). Numerical investigation of geosynthetic-reinforced soil bridge abutments under static loading. *J. Geotech. Geoenviron. Engng* **142**, No. 5, 04016004, https://doi.org/10.1061/(ASCE)GT.1943-5606.0001452.

Zornberg, J. G., Sitar, N. & Mitchell, J. K. (1998a). Performance of geosynthetic reinforced slopes at failure. *J. Geotech. Geoenviron. Engng, ASCE* **124**, No. 8, 670–683.

Zornberg, J. G., Sitar, N. & Mitchell, J. K. (1998b). Limit equilibrium as basis for design of geosynthetic reinforced slopes. *J. Geotech. Geoenviron. Engng, ASCE* **124**, No. 8, 684–698.